

Ram Pressure Stripping in the Virgo Cluster

C. Verdugo¹, F. Combes^{1,2}, K. Dasyra^{1,3}, P. Salomé¹ and J. Braine⁴

¹ Observatoire de Paris, LERMA (CNRS:UMR8112), 61 Av. de l'Observatoire, F-75014, Paris, France e-mail: celia.verdugo@obspm.fr

² Collège de France, 11 Place Marcelin Berthelot, 75005 Paris, France

³ Department of Astrophysics, Astronomy & Mechanics, Faculty of Physics, University of Athens, Panepistimiopolis Zografos 15784, Greece

⁴ Univ. Bordeaux, Laboratoire d'Astrophysique de Bordeaux, (CNRS:UMR5804) 33270 Floirac, France

Received 2015; accepted 2015

ABSTRACT

Gas can be violently stripped from their galaxy disks in rich clusters, and be dispersed over 100kpc-scale tails or plumes. Young stars have been observed in these tails, suggesting they are formed in situ. This will contribute to the intracluster light, in addition to tidal stripping of old stars. We want to quantify the efficiency of intracluster star formation. We present CO(1–0) and CO(2–1) observations, made with the IRAM-30m telescope, towards the ram-pressure stripped tail northeast of NGC4388 in Virgo. HII regions found all along the tails, together with dust patches have been targeted. We detect molecular gas in 4 positions along the tail, with masses between 7×10^5 to $2 \times 10^6 M_{\odot}$. Given the large distance from the NGC 4388 galaxy, the molecular clouds must have formed in situ, from the HI gas plume. We compute the relation between surface densities of star formation and molecular gas in these regions, and find that the star formation has very low efficiency. The corresponding depletion time of the molecular gas can be up to 500 Gyr and more. Since this value exceeds a by far Hubble time, this gas will not be converted into stars, and will stay in a gaseous phase to join the intracluster medium.

Key words. Galaxies: evolution — Galaxies: clusters: Individual: Virgo — Galaxies: clusters: intracluster medium — Galaxies: interactions — Galaxies: ISM

1. Introduction

In overdense cluster environments, galaxies are significantly transformed, through different tidal interactions, like the ones due to other galaxies, the cluster as a whole (e.g. Merritt 1984, Tonnesen et al. 2007), and the ones with the intra-cluster medium (ICM), which strips them from their gas content. This ram-pressure stripping (RPS) process has been described by Gunn & Gott (1972) and simulated by many groups (Quilis et al. 2000, Vollmer et al. 2001, Roediger & Hensler 2005; Jáchym et al. 2007). Evidence of stripping has been observed in many cases (Kenney et al. 2004; Chung et al. 2007; Sun et al. 2007, Vollmer et al. 2008). RPS and/or tidal interactions can disperse the interstellar gas (ISM) of galaxies at large distance, up to 100kpc scales, as shown by the spectacular tail of ionized gas in Virgo (Kenney et al. 2008).

What is the fate of the stripped gas? According to the time-scale of the ejection, the relative velocity of the ICM-ISM interaction, and the environment, it could be first seen as neutral atomic gas (Chung et al. 2009, Scott et al. 2012, Serra et al. 2013), then ionized gas detected in H α (Gavazzi et al. 2001, Cortese et al. 2007, Yagi et al. 2007, Zhang et al. 2013), and is finally heated to X-ray gas temperatures (e.g. Machacek et al. 2005, Sun et al. 2010). In rarer cases, it can be seen as dense and cold molecular gas, detected as carbon monoxide (CO) emission (Vollmer et al. 2005, Dasyra et al. 2012, Jáchym et al. 2014). The presence of these dense molecular clumps might appear surprising, since the RPS should not be able to drag them out of their galaxy disks (Nulsen 1982; Kenney & Young 1989). However

they could reform quickly enough in the tail. The survival of these clouds in the hostile ICM environment, with temperature 10^7 K and destructive X-rays (e.g., Machacek et al. 2004; Fabian et al. 2006; Tamura et al. 2009) is a puzzle, unless they are self-shielded (e.g. Dasyra et al. 2012, Jáchym et al. 2014). The presence of cold molecular gas is also observed in rich galaxy clusters, with cool cores. Here also a multi-phase gas has been detected, in CO, H α , X-rays and also the strongest atomic cooling lines (Edge et al. 2010). Ionized gas, together with warm atomic and molecular gas and cold molecular gas clouds coexist in spatially resolved filaments around the brightest cluster galaxy, such as in the spectacular prototype Perseus A (Conselice et al. 2001; Salomé et al. 2006, 2011; Lim et al. 2012).

The survival of molecular clouds was also observed by Braine et al. (2000) in several tidal tails, and in particular in the interacting system Arp 105 (dubbed the Guitar), embedded in the X-ray emitting medium of the Abell 1185 cluster (Mahdavi et al. 1996). Again, the formation in situ of the molecular clouds is favored (Braine et al. 2000). In the Stephan's Quintet compact group, where X-ray gas and star formation have been observed in between galaxies (O'Sullivan et al. 2009), the shock has been so violent (1000 km/s) that H₂ molecules are formed and provide the best cooling agent, through mid-infrared radiation (Cluver et al. 2010). In this shock, multi-phases of gas coexist, from cold dense molecular gas to X-ray gas.

Does this gas form stars? In usual conditions, inside galaxy disks, the star formation is observed to depend on the amount of molecular gas present (e.g. Bigiel et al. 2008; Leroy et al. 2013). A Schmidt-Kennicutt (S-K) relation is observed, roughly linear, between the surface densities of star formation and molecular

Send offprint requests to: C. Verdugo

gas, leading to a depletion time-scale ($\tau_{\text{dep}} = \Sigma_{\text{gas}}/\Sigma_{\text{SFR}}$) of 2 Gyr. But this relation does not apply in particular regions or circumstances, such as galaxy centers (Casasola et al. 2015), outer parts of galaxies and extended UV disks (Dessauges-Zavadsky et al. 2014), or low surface brightness galaxies (Boissier et al. 2008). Little is known on star formation in gas clouds stripped from galaxies in rich clusters. Boissier et al. (2012) have put constraints on this process, concluding to a very low star formation efficiency, lower by an order of magnitude than what is usual in galaxy disks, and even lower than outer parts of galaxies or in low surface brightness galaxies. It is interesting to better constrain this efficiency, given the large amount of intracluster light (ICL) observed today (e.g. Feldmeier et al. 2002, Mihos et al. 2005). These stars could come from tidal stripping of old stars formed in galaxy disks, or also a large fraction could have formed in situ, from ram-pressure stripped gas. More intracluster star formation could have formed in the past (DeMaio et al. 2015). The origin of the ICL could bring insight on the relative role of galaxy interactions during the cluster formation, or cluster processing after relaxation.

1.1. The tail northeast of NGC4388

One of the environments to probe the survival of molecular gas and the efficiency of star formation under extreme ram-pressure conditions is the RPS tail north of NGC 4388 in the Virgo cluster south of M86, where X-ray gas has been mapped (Iwasawa et al. 2003) and young stars have been found (Yagi et al. 2013). It is located at about 400 kpc in projection from the cluster center M87. NGC 4388 is moving at a relative velocity redshifted by 1500 km/s with respect to M87, and more than 2800 km/s with respect to the M86 group. This strong velocity may explain the violent RPS, the high HI deficiency of NGC 4388 (Cayatte et al. 1990) and the large (~ 35 kpc) emission-line region found by Yoshida et al. (2002), northeast of the galaxy. The ionized gas has a mass of $10^5 M_{\odot}$, and is partly excited by the ionizing radiation of the Seyfert 2 nucleus in NGC 4388. The RPS plume is even more extended in HI (Oosterloo & van Gorkom 2005), up to 110 kpc, with a mass of $3.4 \times 10^8 M_{\odot}$. Gu et al. (2013) have found neutral gas in absorption in X-ray, with column densities $2\text{-}3 \times 10^{20} \text{ cm}^{-2}$, revealing that the RPS tail is in front of M86. The high ratio between hot and cold gas in the clouds means that significant evaporation has proceeded. Yagi et al. (2013) find star-forming regions in the plume at 35 and 66 kpc from NGC 4388, with solar metallicity and age 6 Myrs. Since these stars are younger than the RPS event, they must have formed in situ.

In the present paper we present CO detections in the ram-pressure stripped gas northeast of NGC 4388. In a previous paper, we have already found molecular gas in a ionized gas tail south of M86 (Dasyra et al. 2012), and discussed its survival conditions. We here study the link between new stars formed and molecular gas, to derive the star formation efficiency. In the RPS plume, a significant fraction of the $\text{H}\alpha$ emission could originate from the ionized gas in the outer layers of molecular clouds (Ferland et al. 2009). This makes the $\text{H}\alpha$ lumps good tracers of star formation in an RPS tail, to probe the efficiency of the process of formation of intracluster stars. Section 2 presents the IRAM-30m observations, Section 3 the results obtained, which are discussed in Section 4.

In the following, we assume a distance of 17.5 Mpc to the Virgo cluster (Mei et al. 2007).

2. Observations and data reduction

CO observations along the HI plume (Oosterloo & van Gorkom 2005) connecting NGC4388 and M86 were done with the IRAM 30-m telescope at Pico Veleta, Spain, in two separate runs. The first run was part of the project 195-13, with 28 hours of observation, and took place between the 5th and 8th of December 2013, with excellent weather conditions ($\tau < 0.1$ and a pwv between 0.1 and 3mm). The second run was project 075-14, with 47 hours of observations between June 25th-30th 2014, and had poor to average weather conditions (τ between 0.2 and 0.6 and a pwv between 3 and 10 mm).

All observations were done with the EMIR receiver in the E0/E2 configuration, allowing us to observe simultaneously CO(1–0) and CO(2–1) at 115.271 and 230.538 GHz respectively. The telescope half-power beam widths at these frequencies are $22''$ and $11''$ respectively. The observing strategy consisted in single ON+OFF pointings per each target, with wobbler switching.

Targets along the HI plume were selected for having a match of HI (using the N_{HI} map from Oosterloo & van Gorkom 2005), $\text{H}\alpha$ (with data from Kenney et al. 2008 and Yagi et al. 2013) and 250μ emission (HERSCHEL SPIRE data from Davies et al. 2012). See Figure 1. With this criteria 6 targets were selected for the first run 195-13, and are listed in Table 1 (first 6 rows). As a result of this run, only two sources showed CO detection: Source-1 and HaR-2. Since HaR-2 is of particular interest for being so far away from both galaxies and for having a strong $\text{H}\alpha$ detection (Yagi et al. 2013), it was chosen as a central target around which other 5 extra targets were selected for the second run 075-14 (second half of Table 1), following the path of an HI peak (Figure 1 top right box)

Table 1. Targets and Observations

Source	RA(J2000) [<i>hr,m,s</i>]	DEC(J2000) [<i>deg,m,s</i>]	hel. vel. [km/s]	ON+OFF [hrs]
Source-1	12:26:01.3	12:42:30.1	+2500	4.2
Source-2	12:26:04.9	12:45:16.7	+2500	2.9
Source-3	12:26:25.4	12:50:53.6	+2200	3.1
Source-5	12:26:24.5	12:58:14.6	+2000	3.9
HaR-2	12:26:13.7	12:51:36.9	+2230	7.2
HaR-3-4	12:26:13.5	12:43:03.7	+2500	3.8
HaR-2-1	12:26:16.9	12:53:55.6	+2230	4.5
HaR-2-2	12:26:16.9	12:53:19.3	+2230	5.6
HaR-2-3	12:26:16.9	12:52:43.1	+2230	6.2
HaR-2-4	12:26:15.5	12:52:01.1	+2230	8.0
HaR-1	12:26:14.6	12:51:46.4	+2230	3.8
NGC4388	12:25:46.6	12:39:44.0	+2550	1.2

Notes. Sources in the first 6 rows correspond to run 195-13, and last 6 rows to run 075-14 (although source HaR-2 was observed in both runs). NGC4388 was observed for calibration purposes. Heliocentric velocities are referencial, taken from Oosterloo & van Gorkom (2005) along the HI plume.

Concerning the spectral resolution of our data, during the observations both FTS and WILMA backends were used, simultaneously. The FTS backend has a spectral resolution of 195 kHz and a bandwidth of 32 GHz including both polarizations. At 115 GHz these values correspond to 0.5 and 83200 km/s, and at 230 GHz to 0.25 and 41600 km/s. As for the WILMA backend, we obtained a spectral resolution of 2 MHz and a bandwidth of 16 GHz. At 115 GHz this translates to 5.2 and 41600 km/s, and to 2.6 and 20800 km/s at 230 GHz.

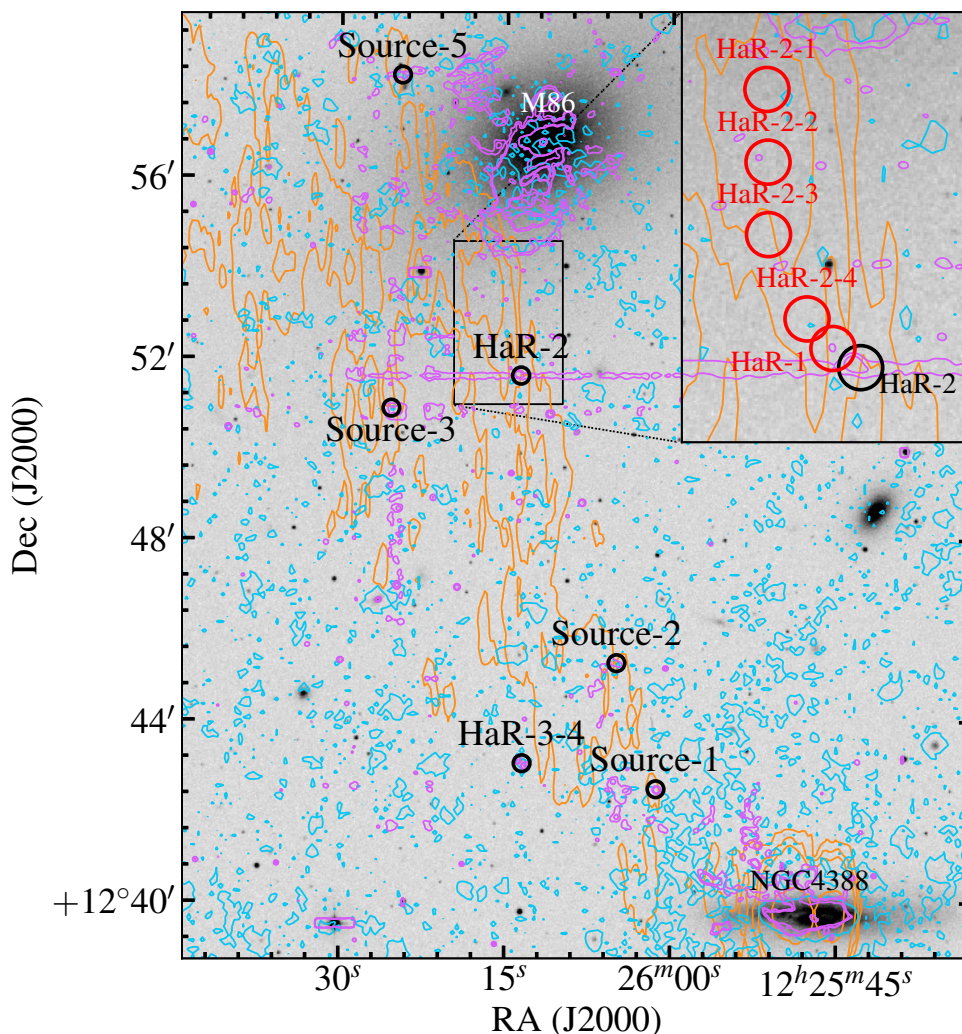


Fig. 1. Targets observed in the Virgo Cluster. Orange: HI contours levels at 1, 5, 10 and $50 \times 10^{19} \text{ cm}^{-2}$ from Oosterloo & van Gorkom (2005), showing the plume of atomic gas stripped from NGC4388. Purple: $\text{H}\alpha$ contours levels at 5, 11 and $50 \text{ e}^-/\text{sec}$ (Kenney et al. 2008). Cyan: $250 \mu\text{m}$ contour levels at 0.01 and 0.1 Jy/beam (Davies et al. 2012). In zoomed regions: targets selected close to HaR-2 for run 075-14 (red circles). Circles enclosing targets are $22''$ width, as the CO(1–0) HPBW.

The data were reduced using the CLASS software from the GILDAS package. First, a careful inspection of all scans was done, to remove the bad ones. The approved scans of the same source, CO line and backend were averaged with a normal time weighting, to obtain one spectrum. Then, each spectrum was inspected individually, and in both of its polarizations, to identify a possible CO emission line. If a detection was found in the spectra of both backends, the best spectrum was chosen (in terms of spectral resolution and S/N) as the final one. The selected spectra with CO emission are presented in Figures 2 and 3, which contain both polarizations, horizontal and vertical, combined.

Baselines were subtracted with polynomials of order 0 and 1 depending on the source, and antenna temperatures were corrected by the telescope beam and forward efficiencies¹ to obtain main beam temperatures. Spectra were smoothed with the han-

ning method to degrade the velocity resolution until obtaining a value no greater than 1/3 of the FWHM line.

Finally, a simple gaussian line was fitted to the line candidate. The CLASS fit return the velocity position of the line, its FWHM, the peak temperature and the integrated line intensity.

Such spectra and fitting results for sources with CO detection are presented in Figures 2 (from the first run) and 3 (from second run) and then in Table 2. For the rest of the sources, with no visible CO detections, 3σ upper limits for I_{CO} where calculated from their rms values, assuming a $\Delta v = 30 \text{ km/s}$. Such limits are presented in Table 3.

3. Results

After selecting the final spectra for every source with a visible detection and fitting their gaussian profiles, line parameters are calculated and presented in Table 2. These CO detections

¹ <http://www.iram.es/IRAMES/mainWiki/Iram30mEfficiencies>

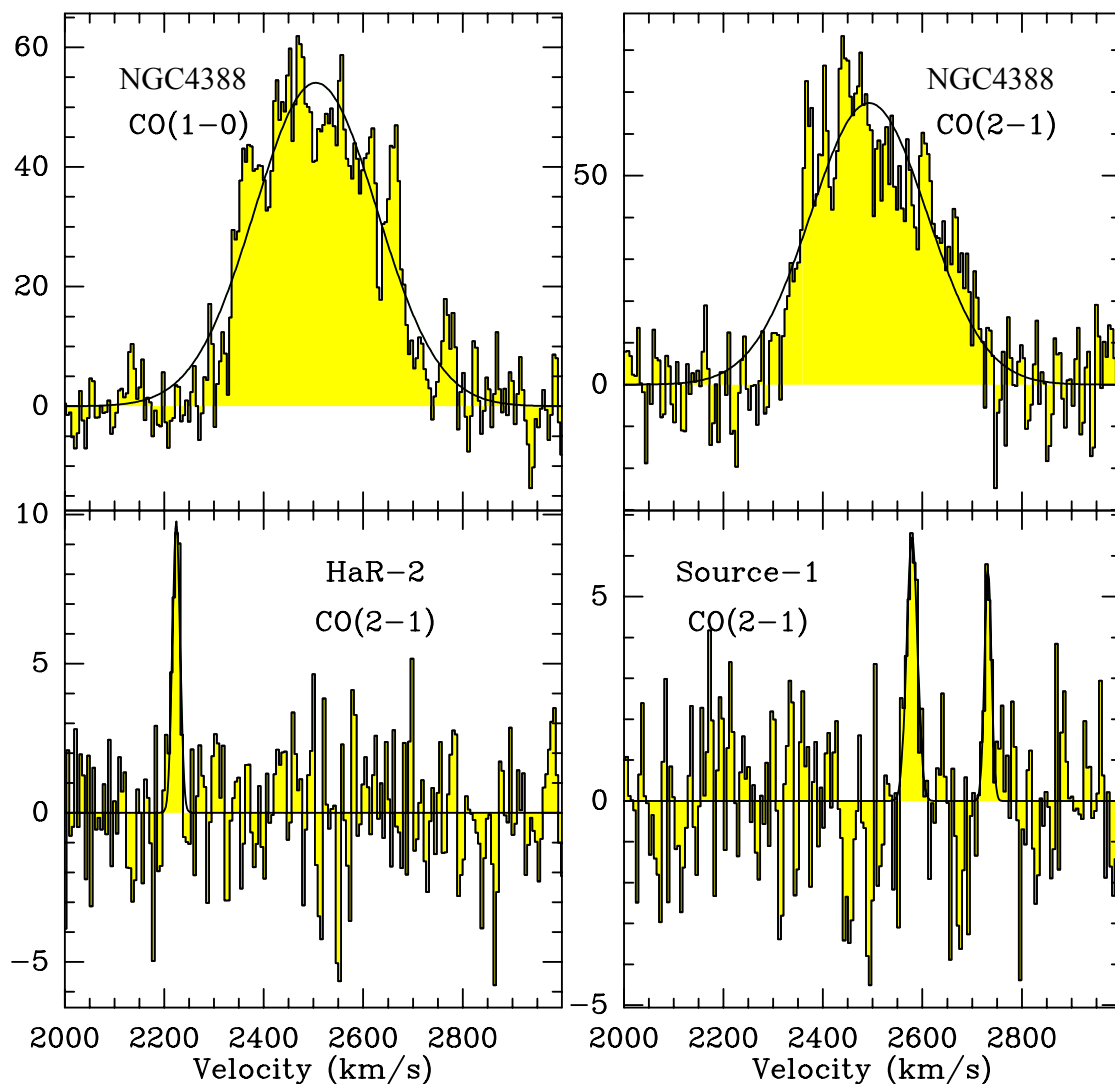


Fig. 2. Top: Spectra taken at the center of NGC4388, observed for calibration purposes. Bottom: Spectra from observing run 195-13 that showed CO emission. Spectra information and line parameters are presented in Table 2. The temperature scale corresponds to main beam temperature in mK.

present velocity centroids in the range of ~ 2200 - 2500 km/s, and are quite consistent with the HI velocities from Table 1, taken from Oosterloo & van Gorkom 2005 (their Fig. 2). H_2 masses were derived from the CO(1-0) line intensity, using a Galactic CO conversion factor of $2.0 \times 10^{20} [\text{cm}^{-2} (\text{K km/s})^{-1}]$ and a correction factor of 1.36 to account for heavy elements:

$$M_{H_2} [M_\odot] = 4.4\pi R^2 [\text{pc}] I_{CO(1-0)} [\text{K km/s}] \quad (1)$$

where the source's radius R corresponds to the CO(1-0) beamsize radius at the distance of the source (17.5 Mpc from Mei et al. 2007).

3.1. Star formation efficiency

To estimate how fast is the gas being transformed into stars, we compare the SFR surface density versus the gas surface density in a S-K relation, to understand the efficiency of this star formation process. Since these are low gas density regions, we can expect a large amount of gas in atomic phase, greater than in molecular phase. Therefore both components, atomic and

molecular, need to be taken into account when estimating a total amount of gas to be converted into stars.

Molecular gas can be directly estimated from the CO(1-0) line intensity, obtained from our observations. If we take Eq. 1, and we divide it by the source area (πR^2), we obtain the H_2 surface density:

$$\Sigma_{H_2} [M_\odot \text{pc}^{-2}] = 4.4 I_{CO(1-0)} [\text{K km s}^{-1}] \quad (2)$$

These values are listed in column 2 of Table 4 for the sources with CO(1-0) detections, including upper limits for the sources with no CO detection using Table 3.

For the atomic gas component, we estimated the amount of HI from the HI column density map of the NGC4388 plume from Oosterloo & van Gorkom (2005). The atomic gas mass is derived from the integrated amount of N_{HI} inside the source solid angle:

$$M_{\text{HI}} = \mu_{\text{mH}} \int N_{\text{HI}} dA = \mu_{\text{mH}} D^2 \int N_{\text{HI}} d\Omega \quad (3)$$

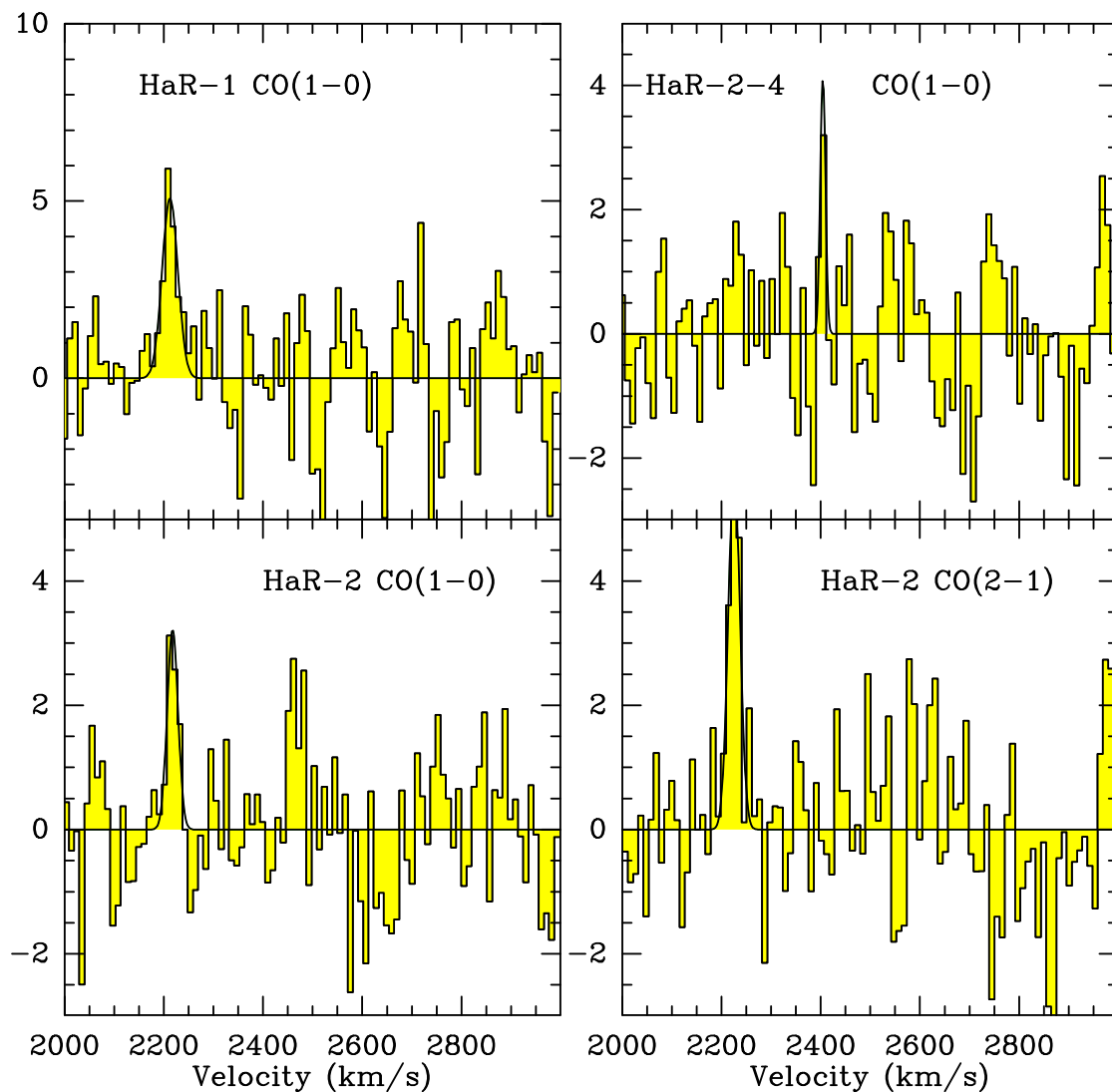


Fig. 3. Final CO spectra for HaR-2, HaR-1 and HaR-2-4 from run 075-14. Only HaR-2 in CO(2–1) has data combined from both runs. All spectra have both polarizations combined. Spectra information and line parameters are presented in Table 2. The temperature scale corresponds to main beam temperature in mK.

Aperture photometry was done in the N_{H} map of Oosterloo & van Gorkom (2005) to obtain the integrated column densities for our sources. We used $22''$ apertures to be consistent with our CO(1–0) observations. Since these apertures are smaller than the spatial resolution of the HI map (18×95.1 arcsec), the photometry results are equivalent to the pixel value of the HI map at the position of our CO targets. These values are listed in column 3 of Table 4. Then, by dividing Eq. 3 by the CO(1–0) beam solid angle $\Omega = \pi R^2$, we obtain the HI surface densities Σ_{HI} listed in column 4 of Table 4.

Finally, we estimate the SFR surface density Σ_{SFR} directly from the H_{α} emission in these regions. From Kennicutt & Evans (2012):

$$\log \text{SFR}[\text{M}_{\odot}\text{yr}^{-1}] = \log L_{H_{\alpha}}[\text{erg s}^{-1}] - 41.27 \quad (4)$$

which, divided by the CO(1–0) beam solid angle Ω , gives the SFR surface density Σ_{SFR} . H_{α} luminosities for HaR-1, HaR-2 and HaR-3-4 were obtained from Yagi et al. (2013), and are listed in Table 4, along with the corresponding Σ_{SFR} . For the remaining sources we used the H_{α} map from Kenney et al. (2008),

using an aperture photometry of $\sim 1''$ in diameter, similar to the seeing of the H_{α} observations from Yagi et al. (2013). For the sources with no visible detection in this map, an upper limit was calculated from the noise level of Kenney’s map, estimated in $4.8 \times 10^{-7} \text{erg s}^{-1} \text{cm}^{-2} \text{sr}^{-1}$.

The SFR surface densities are plotted as a function of the gas surface densities to construct a S-K relation in Figure 4, using the values from Table 4. We have plotted separately, the atomic and molecular gas component of Σ_{gas} , along with the combination of both, in red, black and blue markers respectively. Arrows denote the upper limits values from Table 4. In this Figure, adapted from Jáchym et al. (2014), we can compare our sources with theirs in the Norma Cluster, as well as with the sample of spiral galaxies from Bigiel et al. (2008) (in coloured contours), and the sample of 30 nearby galaxies from Bigiel et al. (2011), plotted as the running medians of Σ_{SFR} as a function of Σ_{H_2} , and with a typical depletion time of ~ 2.3 Gyr. Additionally, shaded regions have been included to represent regions from the outskirts of XUV disk galaxies. NGC4625 and NGC6946 data was taken from Watson et al. (2014) (priv. communication), including IRAM-30m CO observations, and H_{α} luminosities measured

Table 2. CO detections and their line parameters.

Source	line	backend	int. time [min]	v_0 [km/s]	FWHM [km/s]	resol. [km/s]	T_{mb} [mK]	rms [mK]	I_{CO} [mK km/s]	M_{H_2} [$10^6 M_\odot$]
HaR-2	CO(2–1)	FTS	268	2224±2	18±3	4	9.8	2.0	186±29	
Source-1(1)	CO(2–1)	WILMA	232	2579±2	25±5	5	6.4	1.7	173±29	
Source-1(2)	CO(2–1)	WILMA	232	2732±2	16±5	5	5.6	1.7	99±25	
HaR-2	CO(1–0)	WILMA	318	2218±4	26±7	10	3.2	1.5	88±25	1.1
	CO(2–1)	WILMA	586	2226±2	24±6	10	6.3	1.6	163±29	
HaR-1	CO(1–0)	WILMA	229	2212±4	35±13	10	5.2	2.3	199±54	2.4
HaR-2-4	CO(1–0)	WILMA	665	2404±2	12±3	10	4.0	1.4	54±16	0.7
NGC4388	CO(1–0)	WILMA	87	2505±2	289±5	5	54.0	4.8	17000±276	205
	CO(2–1)	WILMA	82	2493±4	275±7	5	67	8.9	20000±490	

Notes. First three rows correspond to observing run 195-13. Both components shown in Figure 2 for Source-1 are listed. H_2 masses were calculated as $M_{H_2} [M_\odot] = 4.4\pi R^2 [pc] I_{CO} [K km/s]$, which uses a Galactic CO conversion factor of $2.0 \times 10^{20} [cm^{-2} (K km/s)^{-1}]$ and a correction factor of 1.36 to account for heavy elements. A distance to the Virgo Cluster of 17.5 Mpc (Mei et al. 2007) was used to calculate the CO(1–0) beam radius as source radius. HaR-2 includes data taken in the first run only for CO(1–0), and data combined from both runs for CO(2–1).

Table 3. CO(1–0) upper limits at 3σ for sources with no detection.

Source	int. time [min]	rms mK	I_{CO}^a [K km/s]	M_{H_2} [$10^6 M_\odot$]	Σ_{H_2} [$M_\odot pc^{-2}$]
Source-2	173	1.2	<0.11	<1.21	<0.48
Source-3	186	1.0	<0.09	<0.99	<0.40
Source-5	231	1.2	<0.11	<1.21	<0.48
HaR-3-4	229	1.0	<0.09	<0.99	<0.40
HaR-2-1	269	1.1	<0.10	<1.10	<0.44
HaR-2-2	334	1.1	<0.10	<1.10	<0.44
HaR-2-3	374	0.6	<0.05	<0.55	<0.22

Notes. ^(a) We assumed a Δv of 30 km/s.

Table 4. Schmidt-Kennicutt relation values.

Source	Σ_{H_2} [$M_\odot pc^{-2}$]	$\int N_{HI} d\Omega^a$ [$10^{12} cm^{-2}$]	Σ_{HI} [$M_\odot pc^{-2}$]	$\log(L_{H\alpha})^b$ [erg s ⁻¹]	$\log(\Sigma_{SFR})$ [$M_\odot yr^{-1} kpc^{-2}$]	$\tau_{dep}(H_2)$ [yr]
Source-1	0.93	0.33	0.40	<35.51	<-6.19	$>1.4 \times 10^{12}$
Source-2	<0.48	0.41	0.50	<35.51	<-6.19	—
Source-3	<0.40	0.56	0.68	<35.51	<-6.19	—
Source-5	<0.48	0.60	0.69	37.51	-4.20	$<7.6 \times 10^9$
HaR-2	0.39	2.12	2.5	37.10	-4.61	1.6×10^{10}
HaR-3-4	<0.40	—	—	37.75	-3.96	$<3.6 \times 10^9$
HaR-2-1	<0.44	5.56	6.77	<35.51	<-6.19	—
HaR-2-2	<0.44	5.13	6.24	<35.51	<-6.19	—
HaR-2-3	<0.22	3.67	4.46	<35.51	<-6.19	—
HaR-2-4	0.24	3.08	3.74	<35.51	<-6.19	$>3.7 \times 10^{11}$
HaR-1	0.88	2.05	2.49	35.89	-5.82	5.8×10^{11}

Notes. Surface densities consider a solid angle $\Omega = 2.74 kpc^2$, equivalent to the CO(1–0) beamsize at the distance of the source (17.5 Mpc from Mei et al. 2007).

^(a) from Oosterloo & van Gorkom (2005).

^(b) from Yagi et al. (2013) and Kenney et al. (2008).

within a $6''$ aperture. M63 (NGC5055) data corresponds to the bright UV region located at $1.35r_{25}$ in Dessauges-Zavadsky et al. (2014), with IRAM 30-m CO data, and a SFR measured from the FUV and $24\mu m$ emission.

“Isochrones” of constant star formation efficiencies are also shown to indicate the depletion times of 10^8 , 10^9 and 10^{10} years to consume all the gas, including an additional red isochrone to mark the age of the universe as one Hubble time (i.e. $\tau_{dep} = 13.8 Gyr$).

Contrary to the photometry done in the HI data, the H_α data was not measured in a $22''$ diameter aperture, as the CO(1–0) FWHM, but in an aperture of $1''$ in diameter, similar to the seeing of those observations. Since we are averaging this H_α emission in a $22''$ aperture to calculate the Σ_{SFR} , we could be diluting the real surface density of the gas being converted into stars. To correct for this beam dilution, as a representation we have shifted one of the points in Figure 4 to a fictitious Σ_{H_2} , corresponding to a source’s solid angle of $1''$ in diameter. This correction translates

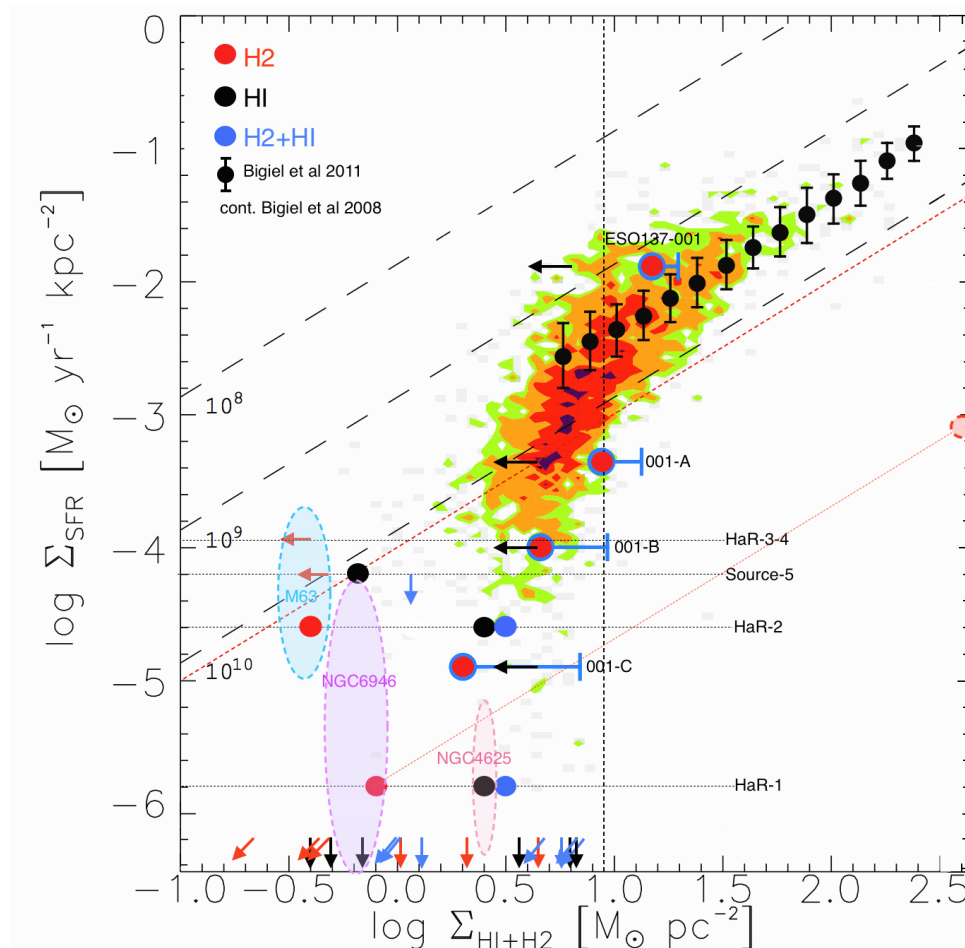


Fig. 4. S-K relation for sources in Table 4, with filled circles and arrows for values and upper limits respectively. Red markers consider only Σ_{H_2} , black ones only HI, and blue ones the sum of both. Figure adapted from Jáchym et al. (2014), where their sources ESO137-001, 001-A, 001-B and 001-C have been plotted in a similar way than ours: red circles for Σ_{H_2} gas, black left arrows for HI upper limits, and blue "error bars" to account for both gas components. Colored contours account for the spiral galaxies from Bigiel et al. (2008) (green, orange, red and purple for 1, 2, 5 and 10 sampling points per 0.05 dex respectively). Black markers with error bars correspond to the running medians in Σ_{SFR} as a function of σ_{H_2} of 30 nearby galaxies from Bigiel et al. (2011). Shaded ovals represent the data from the outer parts of XUV disk galaxies: NGC4625 and NGC6946 from Watson et al. (2014) (priv. communication), and M63 (NGC5055) from Dessauges-Zavadsky et al. (2014), taking only Σ_{H_2} into account in all of them. The dashed vertical line shows the $9 \text{ M}_{\odot} \text{pc}^{-2}$ threshold at which the atomic gas saturates. Dashed inclined lines represent "isochrones" of constant star formation efficiencies, indicating the depletion times $\tau_{\text{dep}} = \Sigma_{\text{gas}}/\Sigma_{\text{SFR}}$ of 10^8 , 10^9 and 10^{10} years to consume all the gas. The dashed red isochrone marks a depletion time equal to the age of the universe, as one Hubble time (13.8 Gyr). A representative shift of the HaR-1 marker for Σ_{H_2} is drawn, to show the "effective" molecular gas density at which stars would be formed in this region if we consider a beam correction factor of +2.68 in log space, to convert our $22''$ beam to a $\sim 1''$ beam as in the H_{α} data.

in a +2.68 shift in log space, and is a representation of the real gas surface density at which stars would be formed, but always with the same τ_{dep} .

For Source-5 we have made the assumption that the HI and $\text{H}\alpha$ emission are spatially correlated, i. e. that they both belong to the gas plume associated to NGC4388. We know that this is true for HI, since we used the data from Oosterloo & van Gorkom (2005) and they probed the physical association of the HI gas plume to NGC4388. But this could not be the case for $\text{H}\alpha$, since we used the data from Kenney et al. (2008) and their $\text{H}\alpha$ map show that this source could be associated to M86 instead, when $\text{H}\alpha$ is considered.

From Figure 4 we can see that our sources have extremely low SFRs in comparison with the nearby spiral galaxies, and are only comparable with the most outer clumps in the $\text{H}_{\alpha}/\text{X}$ -ray tail of the ISM stripped galaxy ESO137-001 in the Norma Cluster (Jáchym et al. 2014) and the XUV disk galaxies from Watson et al. (2014) and Dessauges-Zavadsky et al. (2014). We

obtain depletion times significantly large. For example, HaR-1 and HaR-2 have τ_{dep} values of 2.2×10^{12} and 1.2×10^{11} years respectively, to consume all the amount of gas present ($\text{HI} + \text{H}_2$). These values transform into 1.6×10^{12} and 1.0×10^{11} years if we consider only the atomic gas component, and into 5.8×10^{11} and 1.6×10^{10} years if we consider only the molecular one. Such values are quite large in comparison with the typical τ_{dep} of ~ 2 Gyrs for spiral galaxies, and are even larger than a Hubble time by up to 2 orders of magnitude. In Table 4, depletion times of H_2 that can be calculated are listed in column 7.

The extremely low SF efficiency of our sources seems to fall off the linearity of the S-K relation for typical spiral galaxies at higher gas densities, a result previously reported in other low gas density environments, such as XUV disk galaxies (Dessauges-Zavadsky et al. 2014). Watson et al. (2014) presents a different conclusion for their results in XUVs, with a typical SFR in agreement with the S-K linear regime, but they take into account the $24\mu\text{m}$ emission in the SFR, and neglect the contribution

heavy elements in the Σ_{H_2} . We see that when we correct by these differences to make their data analytically compatible with ours (i.e neglect the $24\mu\text{m}$ emission and correct for heavy elements), their data points in the S-K plot are comparable to ours.

4. Summary and Conclusions

From our molecular cloud and star formation study in the tail north of NGC 4388 in Virgo, we can draw the following conclusions:

1. CO(1–0) and CO(2–1) observations were done with the IRAM 30-m telescope in a total of 11 targets all along the ram-pressure stripped tail northeast NGC4388 in the Virgo Cluster, in order to probe the presence of molecular gas under extreme conditions. Such targets were selected for having strong peaks of HI and H α emission.
2. Four of such positions showed CO detections, and 3 of them concentrated in the HaR-2 region, at a distance of ~ 70 kpc of NGC4388, where molecular gas is unexpected. Given the large distances of these sources to NGC4388, it is not likely that the molecular gas was stripped from the galaxy, and must have formed in situ from the HI gas plume.
3. Gaussian line profiles were fitted to the spectra of the detections, finding a range of velocity dispersion between 12 and 35 km/s. The CO(1–0) line profiles were used to estimate molecular gas masses and surface densities. The amount of molecular gas in these 3 regions (HaR-1, HaR-2 and HaR-2-4) is very low (between 0.7 and $2.4 \times 10^6 M_{\odot}$), and their H $_2$ surface densities between 0.2 and $0.9 M_{\odot} \text{pc}^{-2}$. These values are well below the HI-H $_2$ threshold, where the gas is mainly atomic and very little is known about the SFR at such low gas densities, hence the importance of these detections.
4. Using complementary data from Yagi et al. (2013) and Kenney et al. (2008) for H α and from Oosterloo & van Gorkom (2005) for HI, we computed Σ_{SFR} and Σ_{HI} to plot, in combination with Σ_{H_2} , a S-K relation. Our sources show an extremely low SFR (up to 2 orders of magnitude lower than for typical spiral galaxies). For example, HaR-1 and HaR-2 have total gas depletion times of 2.2×10^{12} and 1.2×10^{11} years respectively. If we consider just the molecular gas component, these depletion times are 5.8×10^{11} and 1.6×10^{10} years. Furthermore, Source-1 and HaR-2-4 have H $_2$ depletion times even greater than 1.4×10^{12} and 3.7×10^{11} years respectively. These high values of depletion times exceed by far a Hubble time, thus indicating that this molecular gas will not form stars eventually, but remain in a gaseous phase and later join the ICM.
5. From Figure 4 we can see the linearity between the SFR and the gas surface density, so clear at high gas surface densities ($> 9 M_{\odot} \text{pc}^{-2}$) for normal spiral galaxies, cannot be extrapolated to lower densities, below the HI-H $_2$ threshold, where the star formation is extremely inefficient, and the molecular gas, even though present, does not necessarily form stars.

Acknowledgements. We warmly thank the referee for constructive comments and suggestions. Also, the IRAM staff is gratefully acknowledged for their help in the data acquisition. We thank T. Oosterloo and J. Kenney for facilitating important HI and H α data, respectively. F.C. acknowledges the European Research Council for the Advanced Grant Program Number 267399-Momentum. We made use of the NASA/IPAC Extragalactic Database (NED), and of the HyperLeda database. C.V. acknowledges financial support from CNRS and CONICYT through agreement signed on December 11th 2007.

References

- Bigiel, F., Leroy, A., Walter, F., et al. 2008, AJ, 136, 2846
 Bigiel, F., Leroy, A. K., Walter, F., et al. 2011, ApJ, 730, L13
 Boissier, S., Boselli, A., Duc, P.-A., et al. 2012, A&A, 545, A142
 Boissier, S., Gil de Paz, A., Boselli, A., et al. 2008, ApJ, 681, 244
 Braine, J., Lisenfeld, U., Due, P.-A., & Leon, S. 2000, Nature, 403, 867
 Casasola, V., Hunt, L., Combes, F., & Garcia-Burillo, S. 2015, ArXiv e-prints [arXiv:1503.00280]
 Cayatte, V., van Gorkom, J. H., Balkowski, C., & Kotanyi, C. 1990, AJ, 100, 604
 Chung, A., van Gorkom, J. H., Kenney, J. D. P., Crowl, H., & Vollmer, B. 2009, AJ, 138, 1741
 Chung, A., van Gorkom, J. H., Kenney, J. D. P., & Vollmer, B. 2007, ApJ, 659, L115
 Cluver, M. E., Appleton, P. N., Boulanger, F., et al. 2010, ApJ, 710, 248
 Conselice, C. J., Gallagher, III, J. S., & Wyse, R. F. G. 2001, AJ, 122, 2281
 Cortese, L., Marcellac, D., Richard, J., et al. 2007, MNRAS, 376, 157
 Dasysra, K. M., Combes, F., Salomé, P., & Braine, J. 2012, A&A, 540, A112
 Davies, J. I., Bianchi, S., Cortese, L., et al. 2012, MNRAS, 419, 3505
 DeMaio, T., Gonzalez, A. H., Zabludoff, A., Zaritsky, D., & Bradač, M. 2015, MNRAS, 448, 1162
 Dessauges-Zavadsky, M., Verdugo, C., Combes, F., & Pfnegger, D. 2014, A&A, 566, A147
 Edge, A. C., Oonk, J. B. R., Mittal, R., et al. 2010, A&A, 518, L46
 Fabian, A. C., Sanders, J. S., Taylor, G. B., et al. 2006, MNRAS, 366, 417
 Feldmeier, J. J., Mihos, J. C., Morrison, H. L., Rodney, S. A., & Harding, P. 2002, ApJ, 575, 779
 Ferland, G. J., Fabian, A. C., Hatch, N. A., et al. 2009, MNRAS, 392, 1475
 Gavazzi, G., Boselli, A., Mayer, L., et al. 2001, ApJ, 563, L23
 Gu, L., Yagi, M., Nakazawa, K., et al. 2013, ApJ, 777, L36
 Gunn, J. E. & Gott, III, J. R. 1972, ApJ, 176, 1
 Iwasawa, K., Wilson, A. S., Fabian, A. C., & Young, A. J. 2003, MNRAS, 345, 369
 Jáchym, P., Combes, F., Cortese, L., Sun, M., & Kenney, J. D. P. 2014, ApJ, 792, 11
 Jáchym, P., Palouš, J., Köppen, J., & Combes, F. 2007, A&A, 472, 5
 Kenney, J. D. P., Tal, T., Crowl, H. H., Feldmeier, J., & Jacoby, G. H. 2008, ApJ, 687, L69
 Kenney, J. D. P., van Gorkom, J. H., & Vollmer, B. 2004, AJ, 127, 3361
 Kenney, J. D. P. & Young, J. S. 1989, ApJ, 344, 171
 Kennicutt, R. C. & Evans, N. J. 2012, ARA&A, 50, 531
 Leroy, A. K., Walter, F., Sandstrom, K., et al. 2013, AJ, 146, 19
 Lim, J., Ohya, Y., Chi-Hung, Y., Dinh-V-Trung, & Shiang-Yu, W. 2012, ApJ, 744, 112
 Machacek, M., Dosaj, A., Forman, W., et al. 2005, ApJ, 621, 663
 Machacek, M. E., Jones, C., & Forman, W. R. 2004, ApJ, 610, 183
 Mahdavi, A., Geller, M. J., Fabricant, D. G., et al. 1996, AJ, 111, 64
 Mei, S., Blakeslee, J. P., Côté, P., et al. 2007, ApJ, 655, 144
 Merritt, D. 1984, ApJ, 276, 26
 Mihos, J. C., Harding, P., Feldmeier, J., & Morrison, H. 2005, ApJ, 631, L41
 Nulsen, P. E. J. 1982, MNRAS, 198, 1007
 Oosterloo, T. & van Gorkom, J. 2005, A&A, 437, L19
 O’Sullivan, E., Giacintucci, S., Vrtelek, J. M., Raychaudhury, S., & David, L. P. 2009, ApJ, 701, 1560
 Quilis, V., Moore, B., & Bower, R. 2000, Science, 288, 1617
 Roediger, E. & Hensler, G. 2005, A&A, 433, 875
 Salomé, P., Combes, F., Edge, A. C., et al. 2006, A&A, 454, 437
 Salomé, P., Combes, F., Revaz, Y., et al. 2011, A&A, 531, A85
 Scott, T. C., Cortese, L., Brinks, E., et al. 2012, MNRAS, 419, L19
 Serra, P., Koribalski, B., Duc, P.-A., et al. 2013, MNRAS, 428, 370
 Sun, M., Donahue, M., Roediger, E., et al. 2010, ApJ, 708, 946
 Sun, M., Donahue, M., & Voit, G. M. 2007, ApJ, 671, 190
 Tamura, T., Maeda, Y., Mitsuda, K., et al. 2009, ApJ, 705, L62
 Tonnesen, S., Bryan, G. L., & van Gorkom, J. H. 2007, ApJ, 671, 1434
 Vollmer, B., Beckert, T., & Davies, R. I. 2008, A&A, 491, 441
 Vollmer, B., Braine, J., Combes, F., & Sofue, Y. 2005, A&A, 441, 473
 Vollmer, B., Cayatte, V., Balkowski, C., & Duschl, W. J. 2001, ApJ, 561, 708
 Watson, L. C., Martini, P., Lisenfeld, U., et al. 2014, in American Astronomical Society Meeting Abstracts, Vol. 223, American Astronomical Society Meeting Abstracts 223, 454.22
 Yagi, M., Gu, L., Fujita, Y., et al. 2013, ApJ, 778, 91
 Yagi, M., Komiyama, Y., Yoshida, M., et al. 2007, ApJ, 660, 1209
 Yoshida, M., Yagi, M., Okamura, S., et al. 2002, ApJ, 567, 118
 Zhang, B., Sun, M., Ji, L., et al. 2013, ApJ, 777, 122